ARTICLES
https://doi.org/10.1038/s41565-019-0428-8
nature nanotechnology

Injection of oxygen vacancies in the bulk lattice of layered cathodes

Pengfei Yan[1,2,8*], Jianming Zheng[3,8], Zhen-Kun Tang[4,5,8], Arun Devaraj[1], Guoying Chen[6], Khalil Amine[7], Ji-Guang Zhang[3], Li-Min Liu[5*] and Chongmin Wang[1*]

Surfaces, interfaces and grain boundaries are classically known to be sinks of defects generated within the bulk lattice. Here, we report an inverse case by which the defects generated at the particle surface are continuously pumped into the bulk lattice. We show that, during operation of a rechargeable battery, oxygen vacancies produced at the surfaces of lithium-rich layered cathode particles migrate towards the inside lattice. This process is associated with a high cutoff voltage at which an anionic redox process is activated. First-principle calculations reveal that triggering of this redox process leads to a sharp decrease of both the formation energy of oxygen vacancies and the migration barrier of oxidized oxide ions, therefore enabling the migration of oxygen vacancies into the bulk lattice of the cathode. This work unveils a coupled redox dynamic that needs to be taken into account when designing high-capacity layered cathode materials for high-voltage lithium-ion batteries.

One of the bottlenecks for achieving the high energy density of Li-ion batteries is the low attainable cathode energy. Currently, the most commonly used cathode materials, such as $LiMn_2O_4$-based high-voltage spinel and $LiFePO_4$-based olivine, are nearly at their theoretical capacities. In contrast, for cathodes based on layered lithium transition metal oxides (LTMO), only slightly more than half of the theoretical capacities have been utilized, indicating significant potential for further increasing their capacities[1–3]. With the recent discovery of oxygen redox activity in Li-excess LTMOs[4–7], we now realize it might be feasible to access a higher fraction of Li in LTMOs to achieve higher reversible capacity via high-voltage cycling[3,8,9]. However, increasing the battery cycling voltage usually aggravates cathode–electrolyte interfacial reactions and leads to severe capacity and voltage fading[10–13]. The interfacial reaction typically leads to the formation of a Li-ion-blocking solid electrolyte interphase layer[10], consumption of liquid electrolyte[10], surface corrosion and dissolution of the LTMO cathode[10,14] and surface phase transformation[15–18]. These surface-related changes are developed after only a few cycles and are propagated very slowly during subsequent cycles[8,19,20], therefore failing to account for the observed continuous capacity and voltage fading, especially following the triggering of the anionic redox process when cathodes are cycled at high charging cutoff voltages[21]. The lack of understanding of the consequences of triggering an anionic redox is considered to be a major challenge for increasing the capacity of this class of cathode materials[22,23].

In this Article we describe evolution of an LTMO cathode lattice during battery cycling at a high charging cutoff voltage as the anionic redox process is triggered. We used focused ion beam (FIB) liftout techniques (Supplementary Fig. 1) to prepare cross-sectional transmission electron microscopy (TEM) specimens to capture the surfaces and interiors of LTMO cathode particles as battery cycling proceeded. The images show that nanovoid formation and lattice transformation start from the particle surface and gradually propagate towards the centre as the battery is cycled. Computational simulations show that triggering anionic redox processes leads to lowering of both the formation energy of oxygen vacancies and the diffusion barrier of oxidized oxide ions, therefore facilitating inward migration of oxygen vacancies. Our work highlights that, although oxygen anions offer the opportunity to access extra capacity during high-voltage cycling in LTMO cathodes, they also lead to the triggering of a degradation mechanism that is believed to play a significant role during prolonged battery cycling.

Formation of nanovoids in bulk lattice of cathode

The electrochemical performance of a $Li_{1.2}Mn_{0.6}Ni_{0.2}O_2$–Li half-cell is shown in Fig. 1a,b, demonstrating the typical capacity decay and voltage fading phenomenon that occurs during prolonged cycling. In addition to surface-related degradation mechanisms, we clearly observed bulk structural degradation, which is featured by the nucleation and growth of nanovoids in the bulk lattice during the battery cycling, as representatively revealed by cross-sectional scanning TEM high-angle annular dark-field (STEM-HAADF) observations on the $Li_{1.2}Mn_{0.6}Ni_{0.2}O_2$ electrodes with different cycle numbers at a high charge cutoff voltage of 4.8 V (Fig. 1c–f). As shown in Fig. 1c,d, the pristine sample, after FIB slicing, always shows uniform contrast across the entire grain, which corresponds to a well-defined layered structure. In sharp contrast, after 300 cycles the sample shows many black dots within the bulk lattice (Fig. 1e). High-resolution STEM-HAADF imaging reveals that the bulk lattice transformed into a spinel-like structure (Fig. 1f). Coupling STEM-HAADF imaging and quantitative energy-dispersive X-ray spectroscopy (EDS) analysis, we confirmed that the black dots are actually nanovoids because STEM-HAADF is a mass-sensitive imaging technique and EDS mapping (Fig. 1g and Supplementary Fig. 2) shows that the black dots have the same composition as the surrounding material.

[1]Environmental Molecular Sciences Laboratory, Pacific Northwest National Laboratory, Richland, WA, USA. [2]Beijing Key Laboratory of Microstructure and Properties of Solids, Institute of Microstructure and Properties of Advanced Materials, Beijing University of Technology, Chaoyang District, Beijing, China. [3]Energy and Environment Directorate, Pacific Northwest National Laboratory, Richland, WA, USA. [4]College of Physics and Electronics Engineering, Hengyang Normal University, Hengyang, China. [5]School of Physics, Beihang University, Beijing, China. [6]Energy Storage and Distributed Resources Division, Lawrence Berkeley National Laboratory, Berkeley, CA, USA. [7]Chemical Sciences and Engineering Division, Argonne National Laboratory, Argonne, IL, USA. [8]These authors contributed equally: Pengfei Yan, Jianming Zheng, Zhen-Kun Tang. *e-mail: pfyan@bjut.edu.cn; liminliu@buaa.edu.cn; chongmin.wang@pnnl.gov

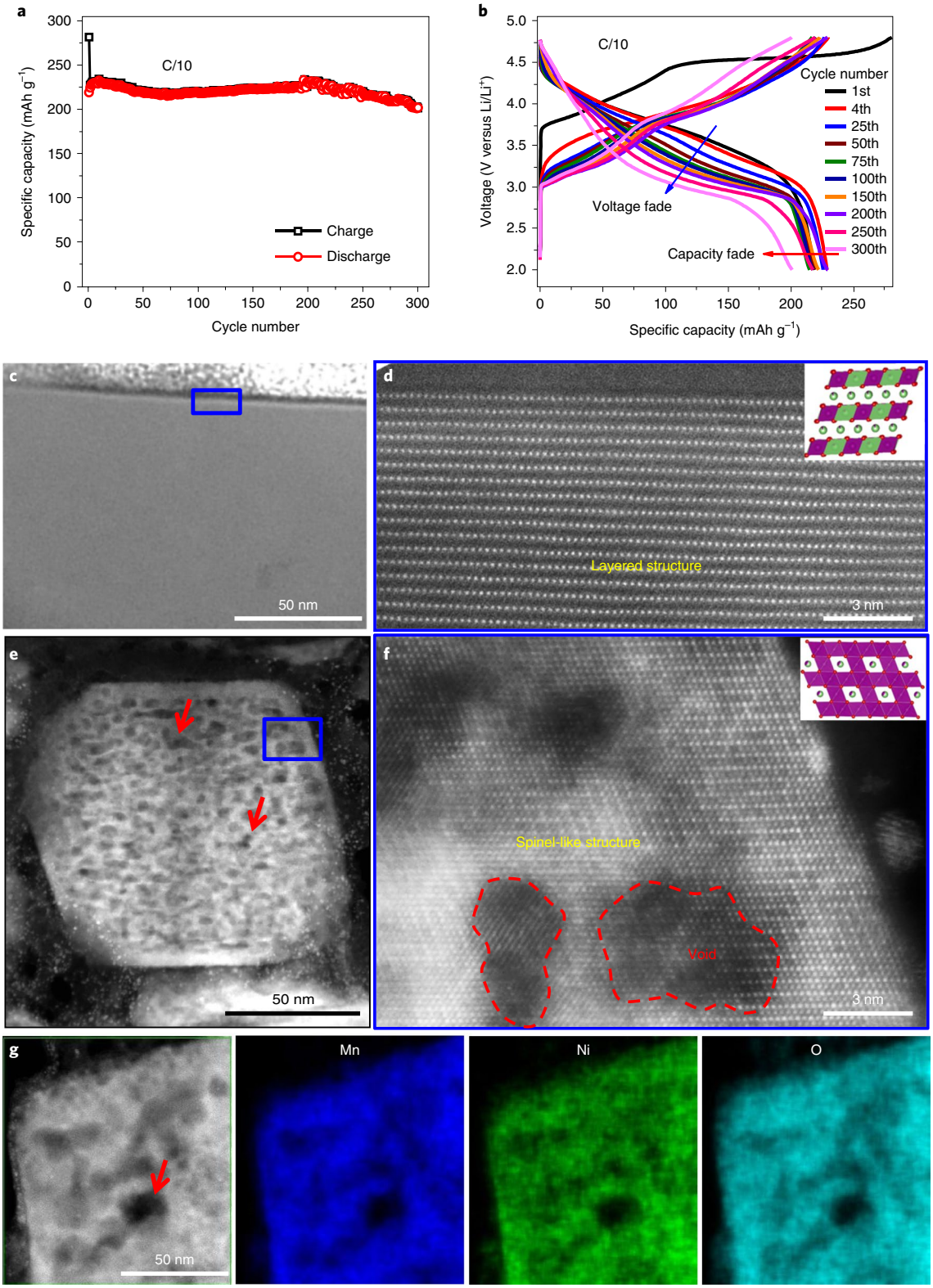

Fig. 1 | Electrochemical performance and structural degradation. The pristine sample shows a uniform and well-defined layered lattice structure. After 300 cycles, nanovoids formed in the interior of the grains as revealed by the black contrasted region, and the lattice is transformed into a spinel-like structure. **a**, Specific capacity as a function of cycle number, revealing capacity fading of the cell using $Li_{1.2}Ni_{0.2}Mn_{0.6}O_2$ as the cathode and Li metal as the anode with a high cutoff voltage of 4.8 V. **b**, Charge–discharge profiles of the $Li_{1.2}Ni_{0.2}Mn_{0.6}O_2$ cathode in a half-cell configuration at different cycle numbers, revealing the voltage and capacity fading. **c**,**d**, STEM-HAADF images of pristine $Li_{1.2}Ni_{0.2}Mn_{0.6}O_2$ at low and high magnifications (the region marked by a blue rectangle in **c** is magnified and shown in **d**), indicating a well-defined layer structure as illustrated by the inset in **d**. **e**,**f**, STEM-HAADF images of a $Li_{1.2}Ni_{0.2}Mn_{0.6}O_2$ cathode after 300 cycles at low and high magnifications (the region marked by a blue rectangle in **e** is magnified and shown in **f**), revealing the formation of nanovoids, shown as dark contrasted spots (indicated by red arrows in **e**), and the lattice transforming to a spinel-like structure (**f**) as illustrated in the inset in **f**. **g**, STEM-HAADF image and EDS elemental maps of Mn, Ni and O, showing no elemental segregation or conglomeration within or around the nanovoids (the red arrow in **g** indicates a nanovoid).

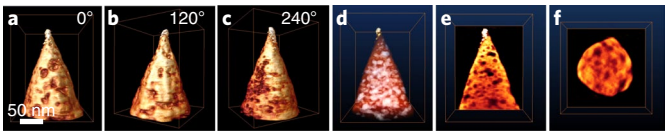

Fig. 2 | 3D tomography reconstruction showing the spatial distribution of nanovoids The needle-shaped specimen was prepared from a $Li_{1.2}Mn_{0.6}Ni_{0.2}O_2$ cathode after 300 cycles at a high cutoff voltage of 4.8 V, revealing many nanovoids present within the grain interior. **a**–**c**, Surface pits resulting from exposure of interior voids when the sample was sectioned. **d**, Visualization of nanovoid distribution within the grain (the white dots represent nanovoids). **e**,**f**, An *x*–*y* ortho slice (**e**) and an *x*–*z* ortho slice (**f**) through the 3D reconstruction, visualizing the nanovoid from different directions. The nanovoids show as black contrasts in **e** and **f**.

Electron energy loss spectroscopy (EELS) analysis performed on the same region (Fig. 1g) indicated that the dark contrasted region shows no Li enrichment. In addition, the EELS thickness map shown in Supplementary Fig. 3 indicates that the dark contrasted region results from mass loss or nanovoid formation. Images from samples (Supplementary Fig. 4) without FIB milling show features similar to those in the corresponding FIB prepared specimens (Fig. 1c–g), thus excluding the possibility that the nanovoid formation and phase transition observed in the cycled samples are due to FIB ion beam damage.

Visualizing nanovoids with 3D reconstruction

Three-dimensional (3D) tomographic imaging confirms that the nanovoids are within the grain bulk and quantitatively reveals their spatial distribution. We prepared a needle-shaped TEM specimen of a $Li_{1.2}Mn_{0.6}Ni_{0.2}O_2$ electrode that had been cycled 300 times at a high charging cutoff voltage of 4.8 V (Supplementary Fig. 5). By collecting a tilting series of STEM-HAADF images ranging from −76° to +78°, we built a 3D tomograph of this grain (Fig. 2a–c). Fragmentation analysis of the tomography data allowed direct visualization of the spatial distribution of the nanovoids in 3D, as shown in Fig. 2d. The 3D volume rendering (Supplementary Video 1) and slicing yielded a visualization of the 3D structure and distribution of the nanovoids. The cross-sectional slices shown in Fig. 2e,f illustrate the nanovoids within the grain, which is further illustrated by the iso-surface plotting of the needle surface shown in Supplementary Video 2. We estimated the nanovoid volume ratio to be 24% for this needle, indicating substantial mass loss and lattice reconstruction during cycling.

Inward propagation of the nanovoid-populated zone

Through systematic observations of the $Li_{1.2}Mn_{0.6}Ni_{0.2}O_2$ electrodes with different cycle numbers, we found that the bulk degradation associated with nanovoid formation is initiated from the particle surface and progressively propagates into the bulk lattice as cycling proceeds. This is shown in Fig. 3, which shows the degradation layer thickness gradually increasing as the cycling number increases. In contrast to the pristine state, after five cycles we observe an obvious change in the particle surface region, where the black dots have formed within a surface layer that is a few nanometres thick (Fig. 3a,b), yet the grain bulk region still retains its original structure. These features are supported by the images shown in Supplementary Fig. 6. After 45 cycles, STEM-HAADF images show the degradation layer becoming much thicker (Fig. 3c,d). Furthermore, the density of the nanovoids gradually increases from the surface to the bulk. High-resolution lattice images (Fig. 3d and Supplementary Fig. 7) from the degradation layer show that the layered structure is heavily disordered due to cation interlayer mixing. After 200 cycles, the thickness of the surface degradation layer further increases (Fig. 3e,f). Because of the increasing thickness of this degradation layer, smaller particles will be fully degraded, as supported by the observation that the nanovoids occur throughout the whole particle, as shown in Fig. 3e.

Concurrent with nanovoid formation and lattice stuctural transformation is the simultaneous loss of oxygen and Li, as revealed by quantitative EDS and qualitative EELS analyses. The STEM-HAADF image of $Li_{1.2}Mn_{0.6}Ni_{0.2}O_2$ cathode particles after 200 cycles in Fig. 4a shows the degraded layer with nanovoids. EDS quantification of the O/Mn ratio along the dashed purple arrow in Fig. 4a is shown in Fig. 4b, demonstrating that the O/Mn ratio is ~2.5 at the outermost surface layer and gradually increases to 3.3 at the inner undegraded region, indicating ~24% oxygen loss at the outermost surface layer. Figure 4c compares the intensities of oxygen from the degradation layer (blue area, Fig. 4a) and the inner undegraded region (red area, Fig. 4a), normalized using the Mn signal intensity; this shows that the oxygen concentration in the degraded region is lower than that in the pristine region. Such chemical composition changes induced by electrochemical cycling are further confirmed after 300 cycles; in fact, as shown in Fig. 4d, the entire grain has been degraded after 300 cycles. By collecting EELS spectra from the whole grain, as shown in Fig. 4e, the low-loss EELS shows that the Li K-edge is significantly lower than that from pristine sample, indicating irreversible loss of Li during cycling, which contributes to cell capacity fading. Furthermore, the depressed oxygen peak shown in Fig. 4f indicates the loss of oxygen, which is further corroborated by EDS analysis (Supplementary Fig. 8), indicating an ~20% oxygen loss for the whole particle after 300 cycles. This finding is consistent with phase transformation from the monoclinic *C*2/*m* ($Li_{1.2}M_{0.8}O_2$) to the defective spinel structure ($Li_xM_2O_4$) as extended cycling occurs[10]. Mn reduction is also shown in Fig. 4f, in which the Mn L_3/L_2 ratio increases significantly after 300 cycles. The structural and chemical evolution observed on the $Li_{1.2}Mn_{0.6}Ni_{0.2}O_2$ cathode particles is also seen on $Li_{1.2}Ni_{0.13}Co_{0.13}Mn_{0.54}O_2$ after 100 cycles at a high charging cutoff voltage of 4.7 V (Supplementary Fig. 9); this confirms that nanovoid formation and lattice transformation are general degradation mechanisms for the Li-rich LTMO.

Anionic redox-mediated vacancy formation and injection

The formation of nanovoids and propagation of the nanovoid populated zone from the surface towards the centre of the particle indicates injection of vacancies from the particle surface into the bulk lattice during battery cycling. Two sources of vacancies can be introduced during electrochemical cycling: Li vacancies and oxygen vacancies. The reversible creation and refilling of Li vacancies via cationic redox in the bulk lattice constitutes the operating principle of Li-ion batteries. Oxygen vacancy generation is realized by oxygen gas evolution and cathode–electrolyte interfacial side reactions, which usually requires a high charge cutoff voltage, typically above 4.5 V for most LTMOs[24–27]. The loss of oxygen, which is similar to the de-intercalation process of Li from the cathode particle, is governed by the oxygen vacancy diffusion rate. However, O^{2-}-mediated oxygen vacancy diffusion has a very high activation energy (1.5 eV)[23,28], indicating that injection of oxygen vacancies through the outward diffusion of O^{2-} is energetically possible but kinetically prohibitive. It is thus believed that only the surface region contains a high concentration of oxygen vacancies and the oxygen vacancy injection rate from surface to bulk should be very low. Therefore, LTMO cathode degradation is intuitively believed to be dominated by surface degradation, while bulk degradation has been overlooked. However, our experimental observations indicate that the mobility of an oxygen vacancy is not as sluggish as it was supposed to be. Therefore, we propose that oxygen vacancy injection is not mediated by O^{2-} but by oxidized oxide ions (indicating an oxide ion is oxidized from valence −2 to form species $(O_2)^{n-}$ ($n = 1, 2, 3$). A theoretical calculation indicates that the energy

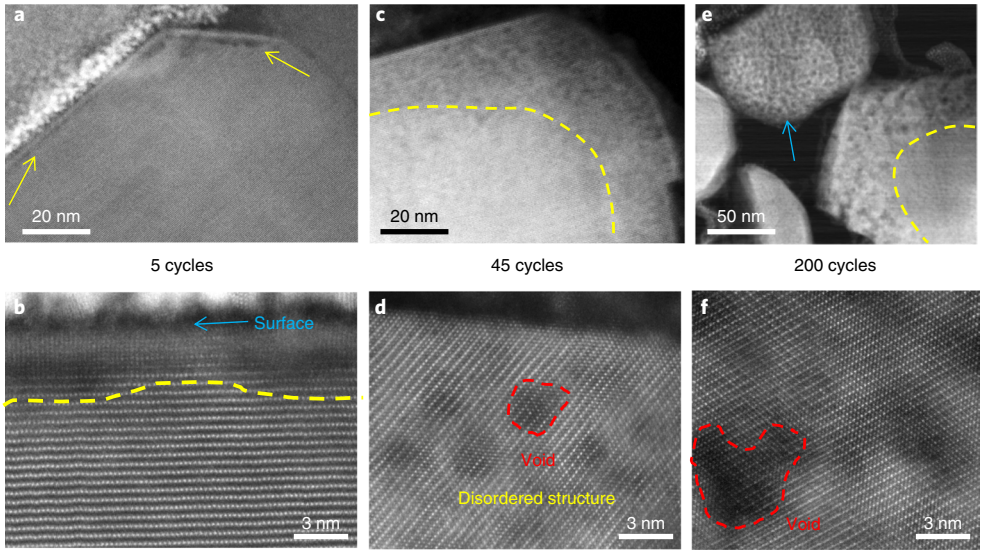

Fig. 3 | Spatial and temporal evolution of structural degradation from the surface into the bulk STEM-HAADF images of the $Li_{1.2}Mn_{0.6}Ni_{0.2}O_2$ cathode show the gradual propagation of the nanovoid-populated zone from the particle surface towards the interior of the particle with increasing cycles of the battery. **a**,**b**, After five cycles, formation of the nanovoid-populated region at the particle surface region is indicated by the yellow arrows in **a**, where the nanovoid shows as a dark contrast. **c**,**d**, After 45 cycles, the nanovoid-populated zone thickens. The red dashed line in **d** indicates a nanovoid. **e**,**f**, After 200 cycles, further thickening of the nanovoid-populated zone occurs. Note that the small particle as indicated by the blue arrow in **e** has been fully populated by nanovoids. The dashed yellow lines in **b**, **c** and **e** mark the boundary between the nanovoid-populated zone near the surface and the region free of nanovoids within the bulk lattice.

barrier for O^{1-} diffusion can be as low as 0.9 eV (ref. [23]), which suggests that if oxidized oxide ions $(O_2)^{n-}$ ubiquitously exist in the Li-excess LTMO, the oxygen vacancy diffusion efficiency can be significantly enhanced. Therefore, injection of oxygen vacancies into the interior of the particle is mediated by the outward diffusion of oxidized oxide ions $(O_2)^{n-}$, which is consistent with the fact that nanovoid formation is directly associated with a high cutoff voltage at which the O^{2-} can be oxidized[29] and is further supported by first-principles calculations. To show the valence changes of both Ni and O atoms during the charging process, the density of state (DOS) and the corresponding empty states in the DOS induced by removing Li atoms are shown in Fig. 5. Figure 5a shows that, when charging the cathode to extract two Li ions, only nickel (Ni) is oxidized to higher valence states, which corresponds to the operation of the cation redox mechanism. Cation redox will terminate when all the Ni ions are oxidized to a 4+ valence state, and further removal of Li ions will trigger the anion redox reaction. According to the configuration of a $Li_{15}Ni_2Mn_7O_{24}$ supercell (Supplementary Fig. 10), the cation redox can only enable the removal of three Li ions, beyond which anion redox will take over. As shown in Fig. 5b, an oxidized oxide ion, namely an oxygen hole, is formed when four Li ions are removed. Figure 5c shows the Ni electronic spin density and corresponding Ni–O octahedron configurations when Ni is at different valence state. We also calculated the formation energy of an oxygen vacancy (V_O) versus Li vacancy (V_{Li}). As shown in Fig. 5d, the V_O formation energy is sharply reduced once anion redox is triggered, meaning that an oxygen hole can promote oxygen vacancy formation.

Accompanying anion-induced vacancy injection is cation migration, which is a short-range process facilitated by oxygen vacancies and reduced valence state. Cation mobility shows a dependence on the species of the cation. Of Ni, Co and Mn, Ni is the most mobile species for migrating to the Li layer, followed by Co and Mn[30,31]. Migration of Ni, Co and Mn into the Li layer will lead to the layer to disordered phase transformation. Previous calculations indicate that the migration energy barrier of Ni in the Li layer is very low[32], so, once Ni ions migrate from the transition metal layer into the Li layer, they will very possibly migrate out of the bulk lattice, leading to the loss of Ni[10,33]; this is consistently supported by the depressed Ni peak shown in Fig. 4c after prolonged cycling. The observed nanovoid formation is a synergetic effect of anion migration and cation redistribution. Accordingly, stabilizing both the anions and cations can effectively suppress unwanted nanovoid formation.

Nanovoid formation via condensation of injected vacancies involves hopping of both cations and anions in the lattice, consequently leading to the following irreversible structural and chemical changes. First, development of a stable V_{Li}–V_O cluster, and eventually the formation of nanovoids, will cause irreversible Li site loss through void sweeping of Li vacancy sites. Second, oxygen vacancies will lead to the reduction of transition metal cations, facilitating their migration to the Li layer and therefore structure transformation within the grain interior[34,35]. The irreversible migration of transition metal to the Li layer has been suggested to be one of the main reasons for voltage fade[36–39]. Finally, redox oxygen species play conflicting roles. On the one hand, oxygen anions can act as redox species to facilitate high capacity in a Li-excess LTMO cathode[6,7,40]. On the other hand, the oxidized oxide ion lowers both the formation energy and diffusion barrier of oxygen vacancies in the lattice, which can significantly enhance oxygen vacancy injection, thus aggravating the bulk lattice degradation of Li-excess LTMO cathodes, as we have shown.

Our study highlights that the surface and bulk degradations are governed by different mechanisms, and each evolves in very different ways during prolonged cycles; however, they also correlate. Surface degradation is kinetically favoured at the beginning, so it plays a dominant role in the first few cycles. After forming a densified surface layer, surface degradation becomes insignificant and bulk degradation turns into the dominant degradation mechanism. Therefore, bulk degradation matters more in terms of long-term cycle stability, especially if a high charging voltage is applied. This electrochemically driven vacancy injection and condensation process is a general degradation mechanism for all cathode materials.

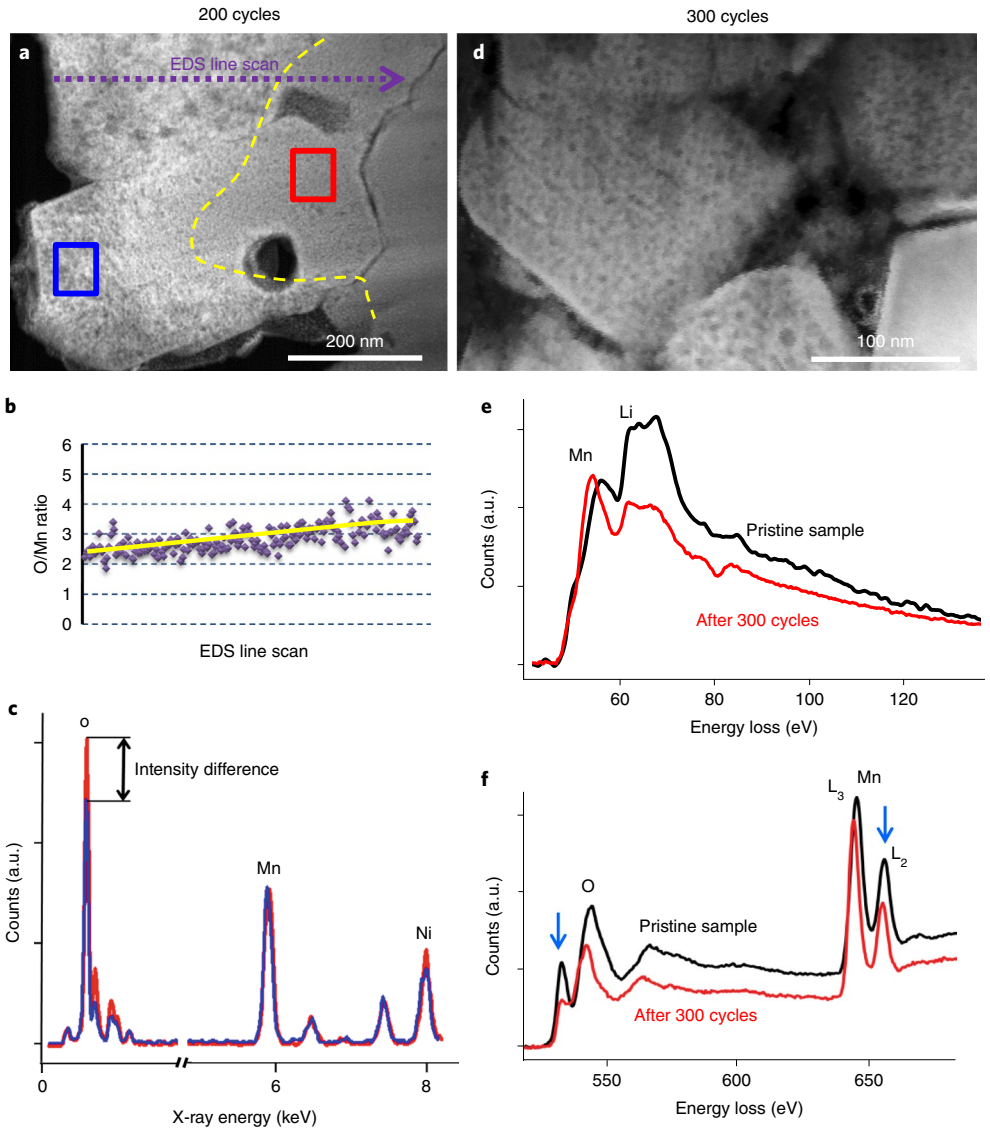

Fig. 4 | Chemical composition analysis. STEM-HAADF images and chemical composition analysis using EDS and EELS to correlate structural degradation with composition in a $Li_{1.2}Mn_{0.6}Ni_{0.2}O_2$ cathode. **a**, After 200 cycles, the dashed yellow line marks the boundary between the zone populated with nanovoids and the region that is free of nanovoids within the bulk lattice. **b**, EDS quantification of the O/Mn ratio along the line scan in **a** from the degraded surface region into the pristine bulk region, revealing a gradient of the O/Mn ratio. **c**, Comparison of EDS spectra captured from two regions, marked with blue and red rectangles in **a**. With scaling of the Mn count at the same intensity, the EDS intensity of both oxygen and nickel captured from the surface degraded region (blue line in **c**) acquired from the blue rectangle in **a** is depressed compared with that captured from the pristine bulk (the red line is acquired from the red rectangle in **a**), indicating the loss of both oxygen and nickel during structural degradation. **d**, As in **a**, but after 300 cycles. **e**, Comparison of the low-loss EELS between the pristine sample and the sample after 300 cycles indicates a depressed Li K-edge intensity after 300 cycles, revealing that the Li concentration in the sample after 300 cycles is lower than that in the pristine sample. **f**, EELS O K-edge and Mn L-edge from the samples before (the pristine sample) and after 300 cycles, showing a depressed O K-edge and Mn L-edge peak after cycling (indicated by blue arrows), demonstrating the structural disordering in the degraded zone.

Note that oxygen vacancies can only be introduced into the bulk lattice via inward diffusion of surface oxygen vacancies. Thus, to control the degradation related to vacancy injection, suppressing surface vacancy generation and blocking the oxygen vacancy inward diffusion path are the two critical approaches. Essentially, the approaches have been verified by (1) introducing a cavity band adjacent to the particle surface to effectively mitigate oxygen evolution[41] and (2) doping the surface to strongly bond oxygen, thus enhancing the cycling stability of the capacity and voltage[42]. Furthermore, our observations of oxygen vacancy injection explain that Mn and Co will gradually transform from inactive to active redox species upon cycling[43], which is a process that contributes to voltage decay but preserves capacity retention.

Conclusions

Our cross-sectional STEM observations and 3D tomography reconstructions offer a unique opportunity for understanding bulk lattice degradation of LTMO cathodes. This bulk degradation involves nanovoid formation and lattice structure transformation, which are consequences of electrochemically driven oxygen vacancy formation at particle surfaces and subsequent injection into the bulk lattice and a condensation process, which is sharply contrasted with the case of a thermally driven process. Although an anionic redox reaction coupled with a cationic redox reaction has been demonstrated to be a new route for developing a high-capacity cathode, excitation of anionic redox-induced lattice instability as revealed in this work indicates

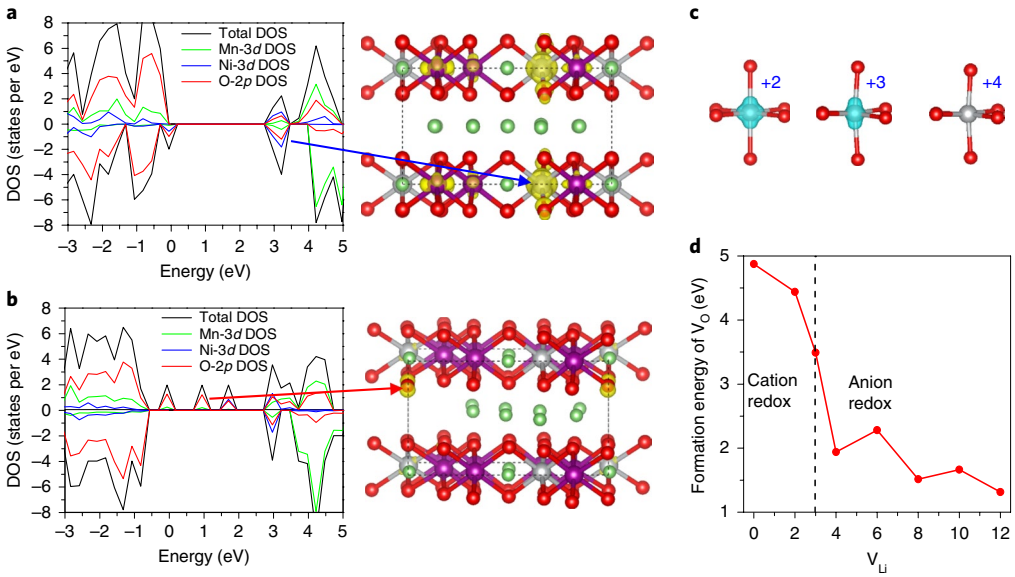

Fig. 5 | First-principles calculation to reveal the triggering of anionic redox. Calculated electronic structure and formation energy of an oxygen vacancy in the charging process. **a**, The DOS after removing two Li ions, which leads to the oxidation of Ni ions, as indicated by the blue arrow. **b**, DOS after removing four Li ions, which leads to the oxidation of oxide ions, as indicated by the red arrow. **c**, Corresponding electronic spin density and valence states of Ni derived from the DOS of the charging process. **d**, The formation energy of an oxygen vacancy as a function of the Li atoms removed from the supercell. The dashed line in **d** indicates the transition point of the valence change from Ni to O during removal of the Li ions. Purple, silver, green and red balls represent Mn, Ni, Li and O atoms, respectively.

the conflicting roles of oxygen redox activity during high voltage cycling. The progressive surface-to-bulk degradation indicates that the suppression of oxygen vacancy generation at the particle surface is the key factor for curtailing subsequent injection of vacancies and, therefore, to achieving better cycling stability of LTMO cathode materials. The findings presented in this Article provide insight into the anionic redox mechanism in a Li-rich layered cathode and will stimulate new thoughts for designing better cathodes with a combination of both cationic and anionic redox processes.

Online content

Any methods, additional references, Nature Research reporting summaries, source data, extended data, supplementary information, acknowledgements, peer review information; details of author contributions and competing interests; and statements of data and code availability are available at https://doi.org/10.1038/s41565-019-0428-8.

Received: 16 September 2018; Accepted: 13 March 2019;
Published online: 22 April 2019

References

1. Rozier, P. & Tarascon, J. M. Review—Li-rich layered oxide cathodes for next-generation Li-ion batteries: chances and challenges. *J. Electrochem. Soc.* **162**, A2490–A2499 (2015).
2. Manthiram, A., Knight, J. C., Myung, S. T., Oh, S. M. & Sun, Y. K. Nickel-rich and lithium-rich layered oxide cathodes: progress and perspectives. *Adv. Energy Mater.* **6**, 1501010 (2016).
3. Hy, S. et al. Performance and design considerations for lithium excess layered oxide positive electrode materials for lithium ion batteries. *Energy Environ. Sci.* **9**, 1931–1954 (2016).
4. Seo, D. H. et al. The structural and chemical origin of the oxygen redox activity in layered and cation-disordered Li-excess cathode materials. *Nat. Chem.* **8**, 692–697 (2016).
5. Luo, K. et al. Charge-compensation in 3D-transition-metal-oxide intercalation cathodes through the generation of localized electron holes on oxygen. *Nat. Chem.* **8**, 684–691 (2016).
6. McCalla, E. et al. Visualization of O–O peroxo-like dimers in high-capacity layered oxides for Li-ion batteries. *Science* **350**, 1516–1521 (2015).
7. Sathiya, M. et al. Reversible anionic redox chemistry in high-capacity layered-oxide electrodes. *Nat. Mater.* **12**, 827–835 (2013).
8. Qiu, B., Zhang, M., Xia, Y., Liu, Z. & Meng, Y. S. Understanding and controlling anionic electrochemical activity in high-capacity oxides for next generation Li-ion batteries. *Chem. Mater.* **29**, 908–915 (2017).
9. Ceder, G. et al. Identification of cathode materials for lithium batteries guided by first-principles calculations. *Nature* **392**, 694–696 (1998).
10. Zheng, J. et al. Structural and chemical evolution of Li- and Mn-rich layered cathode material. *Chem. Mater.* **27**, 1381–1390 (2015).
11. Gu, L., Xiao, D., Hu, Y. S., Li, H. & Ikuhara, Y. Atomic-scale structure evolution in a quasi-equilibrated electrochemical process of electrode materials for rechargeable batteries. *Adv. Mater.* **27**, 2134–2149 (2015).
12. Gu, M. et al. Nanoscale phase separation, cation ordering and surface chemistry in pristine $Li_{1.2}Ni_{0.2}Mn_{0.6}O_2$ for Li-ion batteries. *Chem. Mater.* **25**, 2319–2326 (2013).
13. Xu, B., Fell, C. R., Chi, M. F. & Meng, Y. S. Identifying surface structural changes in layered Li-excess nickel manganese oxides in high voltage lithium ion batteries: a joint experimental and theoretical study. *Energy Environ. Sci.* **4**, 2223–2233 (2011).
14. Zheng, J. et al. Corrosion/fragmentation of layered composite cathode and related capacity/voltage fading during cycling process. *Nano Lett.* **13**, 3824–3830 (2013).
15. Mohanty, D. et al. Structural transformation of a lithium-rich $Li_{1.2}Co_{0.1}Mn_{0.55}Ni_{0.15}O_2$ cathode during high voltage cycling resolved by in situ X-ray diffraction. *J. Power Sources* **229**, 239–248 (2013).
16. Yang, X. Q., Sun, X. & McBreen, J. New findings on the phase transitions in $Li_{1-x}NiO_2$: in situ synchrotron X-ray diffraction studies. *Electrochem. Commun.* **1**, 227–232 (1999).
17. Yoon, W.-S., Chung, K. Y., McBreen, J. & Yang, X.-Q. A comparative study on structural changes of $LiCo_{1/3}Ni_{1/3}Mn_{1/3}O_2$ and $LiNi_{0.8}Co_{0.15}Al_{0.05}O_2$ during first charge using in situ XRD. *Electrochem. Commun.* **8**, 1257–1262 (2006).
18. Rana, J. et al. Structural changes in Li_2MnO_3 cathode material for Li-ion batteries. *Adv. Energy Mater.* **4**, 1300998 (2014).
19. Lin, F. et al. Surface reconstruction and chemical evolution of stoichiometric layered cathode materials for lithium-ion batteries. *Nat. Commun.* **5**, 3529 (2014).
20. Yabuuchi, N., Yoshii, K., Myung, S. T., Nakai, I. & Komaba, S. Detailed studies of a high-capacity electrode material for rechargeable batteries, Li_2MnO_3–$LiCo_{1/3}Ni_{1/3}Mn_{1/3}O_2$. *J. Am. Chem. Soc.* **133**, 4404–4419 (2011).
21. Yan, P. F. et al. Intragranular cracking as a critical barrier for high-voltage usage of layer-structured cathode for lithium-ion batteries. *Nat. Commun.* **8**, 14101 (2017).

22. Pearce, P. E. et al. Evidence for anionic redox activity in a tridimensional-ordered Li-rich positive electrode beta-Li_2IrO_3. *Nat. Mater.* **16**, 580–586 (2017).
23. Lee, E. & Persson, K. A. Structural and chemical evolution of the layered Li-excess Li_xMnO_3 as a function of Li content from first-principles calculations. *Adv. Energy Mater.* **4**, 1400498 (2014).
24. Armstrong, A. R. et al. Demonstrating oxygen loss and associated structural reorganization in the lithium battery cathode $Li[Ni_{0.2}Li_{0.2}Mn_{0.6}]O_2$. *J. Am. Chem. Soc.* **128**, 8694–8698 (2006).
25. Lu, Z. H., Beaulieu, L. Y., Donaberger, R. A., Thomas, C. L. & Dahn, J. R. Synthesis, structure and electrochemical behavior of $Li[Ni_xLi_{1/3-2x/3}Mn_{2/3-x/3}]O_2$. *J. Electrochem. Soc.* **149**, A778–A791 (2002).
26. Hausbrand, R. et al. Fundamental degradation mechanisms of layered oxide Li-ion battery cathode materials: methodology, insights and novel approaches. *Mater. Sci. Eng. B* **192**, 3–25 (2015).
27. Reimers, J. N. & Dahn, J. R. Electrochemical and in situ X-ray diffraction studies of lithium intercalation in Li_xCoO_2. *J. Electrochem. Soc.* **139**, 2091–2097 (1992).
28. Hoang, K. Defect physics, delithiation mechanism, and electronic and ionic conduction in layered lithium manganese oxide cathode materials. *Phys. Rev. Appl.* **3**, 024013 (2015).
29. Gent, W. E. et al. Coupling between oxygen redox and cation migration explains unusual electrochemistry in lithium-rich layered oxides. *Nat. Commun.* **8**, 2091 (2017).
30. Yan, P. et al. Atomic-resolution visualization of distinctive chemical mixing behavior of Ni, Co and Mn with Li in layered lithium transition metal oxide cathode materials. *Chem. Mater.* **27**, 5393–5401 (2015).
31. Yan, P., Zheng, J., Zhang, J.-G. & Wang, C. Atomic resolution structural and chemical imaging revealing the sequential migration of Ni, Co and Mn upon the battery cycling of layered cathode. *Nano Lett.* **17**, 3946–3951 (2017).
32. Gu, M. et al. Conflicting roles of nickel in controlling cathode performance in lithium ion batteries. *Nano Lett.* **12**, 5186–5191 (2012).
33. Yan, P. et al. Evolution of lattice structure and chemical composition of the surface reconstruction layer in $Li_{1.2}Ni_{0.2}Mn_{0.6}O_2$ cathode material for lithium ion batteries. *Nano Lett.* **15**, 514–522 (2015).
34. Qian, D., Xu, B., Chi, M. & Meng, Y. S. Uncovering the roles of oxygen vacancies in cation migration in lithium excess layered oxides. *Phys. Chem. Chem. Phys.* **16**, 14665–14668 (2014).
35. Fell, C. R. et al. Correlation between oxygen vacancy, microstrain and cation distribution in lithium-excess layered oxides during the first electrochemical cycle. *Chem. Mater.* **25**, 1621–1629 (2013).
36. Sathiya, M. et al. Origin of voltage decay in high-capacity layered oxide electrodes. *Nat. Mater.* **14**, 230–238 (2015).
37. Mohanty, D. et al. Unraveling the voltage-fade mechanism in high-energy-density lithium-ion batteries: origin of the tetrahedral cations for spinel conversion. *Chem. Mater.* **26**, 6272–6280 (2014).
38. Abdellahi, A., Urban, A., Dacek, S. & Ceder, G. The effect of cation disorder on the average Li intercalation voltage of transition-metal oxides. *Chem. Mater.* **28**, 3659–3665 (2016).
39. Lee, J. et al. Unlocking the potential of cation-disordered oxides for rechargeable lithium batteries. *Science* **343**, 519–522 (2014).
40. Saubanere, M., McCalla, E., Tarascon, J. M. & Doublet, M. L. The intriguing question of anionic redox in high-energy density cathodes for Li-ion batteries. *Energy Environ. Sci.* **9**, 984–991 (2016).
41. Qiu, B. et al. Gas–solid interfacial modification of oxygen activity in layered oxide cathodes for lithium-ion batteries. *Nat. Commun.* **7**, 12108 (2016).
42. Liu, S. et al. Surface doping to enhance structural integrity and performance of Li-rich layered oxide. *Adv. Energy Mater.* **8**, 1802105 (2018).
43. Hu, E. et al. Evolution of redox couples in Li- and Mn-rich cathode materials and mitigation of voltage fade by reducing oxygen release. *Nat. Energy* **3**, 690–698 (2018).

Acknowledgements

This work was supported by the Assistant Secretary for Energy Efficiency and Renewable Energy, Office of Vehicle Technologies, of the US Department of Energy (DOE) under contract no. DE-AC02-05CH11231, subcontract no. 6951379 under the Batteries for Advanced Battery Materials Research. The work was conducted in the William R. Wiley Environmental Molecular Sciences Laboratory, a national scientific user facility sponsored by DOE's Office of Biological and Environmental Research and located at PNNL. PNNL is operated by Battelle for DOE under contract DE-AC05-76RLO1830. L.-M.L. was supported by the Science Challenge Project (TZ2018004) of the National Natural Science Foundation of China (nos. 51572016 and U1530401) and the Fundamental Research Funds for the Central Universities, and Newton Advanced Fellowship under grant no. NAFR1180242. P.Y. acknowledges support from the National Natural Science Fund for Innovative Research Groups (grant no. 51621003) and the National Key Research and Development Program of China (grant no. 2016YFB0700700). Z.-K.T. thanks the National Natural Science Foundation of China (grant no. 51602092) for support.

Author contributions

P.Y. and C.W. conceived the research plan. J.Z., J.-G.Z., K.A. and G.C. synthesized the samples and carried out the cell test. P.Y. conducted the TEM work. Z.-K.T. and L.-M.L. conducted the simulation work. P.Y. and C.W. wrote the manuscript. All authors approved the final version.

Competing interests

The authors declare no competing interests.

Additional information

Supplementary information is available for this paper at https://doi.org/10.1038/s41565-019-0428-8.

Reprints and permissions information is available at www.nature.com/reprints.

Correspondence and requests for materials should be addressed to P.Y., L.-M.L. or C.W.

Journal peer review information: *Nature Nanotechnology* thanks Jun Chen and the other anonymous reviewer(s) for their contribution to the peer review of this work.

Methods

Material synthesis and electrochemical test. We used a co-precipitation method to synthesize $Li_{1.2}Mn_{0.6}Ni_{0.2}O_2$. A molten-salt method was used to synthesize $Li_{1.2}Ni_{0.13}Co_{0.13}Mn_{0.54}O_2$ (ref. [44]). Electrochemical performance was evaluated in coin-type cells. The cathode electrodes were prepared by coating a slurry containing 80% active mass, 10% Super P and 10% poly(vinylidene fluoride) binder onto an aluminium foil current collector. Coin-type cells were assembled with the as-prepared composite cathode, metallic Li foil as the counter-electrode and reference electrodes, Celgard K1640 monolayer polyethylene membrane as the separator, and 1 M Li hexafluorophosphate ($LiPF_6$) dissolved in ethyl carbonate and dimethyl carbonate (1:2 in volume) as the electrolyte in an argon-filled MBraun glovebox. All cathode materials were cycled at 0.1 C (1 C = 200 mA g^{-1}).

TEM specimen preparation and characterization. FIB/scanning electron microscopy (SEM) imaging and TEM specimen preparation were conducted on an FEI Helios Dual-Beam FIB operating at 2–30 kV. We used a standard liftout procedure to directly prepare thin-section TEM specimens from each electrode foil. First, a 1.2-μm-thick Pt layer (200 nm electron-beam deposition followed by 1 μm ion-beam deposition) was deposited on a region to avoid Ga ion beam damage in the subsequent liftout and thinning process. After liftout, the specimen was thinned to 200 nm using a 30 kV Ga ion beam. Then, a 2 kV final polishing was performed to remove any surface damage until electron transparency at 5 kV SEM imaging was achieved. After the 2 kV Ga ion polish, the surface-damaged layer was less than 1 nm. The needle sample was prepared using FIB-based liftout and annular milling, a procedure that is very similar to that used to prepare samples for atom probe tomography[45]. The annular milling of $Li_{1.2}Mn_{0.6}Ni_{0.2}O_2$ was initially performed at an acceleration voltage of 30 kV. At the the end of annular milling, the Ga acceleration voltage was reduced to 2 kV to eliminate any Ga implantation damage on the top surface of the needle.

The FIB-prepared LTMO samples were examined using an FEI Titan80-300 S/TEM microscope at 300 kV. The microscope was equipped with a probe spherical aberration corrector that enabled sub-ångstrom imaging using STEM-HAADF detectors. For STEM-HAADF imaging, the inner and outer collection angles of the annular dark-field detector were set at 55 and 220 mrad, respectively. STEM-EDS and STEM-EELS were performed on a probe aberration-corrected JEOL JEM-ARM200CF at 200 kV. STEM-EELS data were collected in dual-EESL mode to obtain both zero-loss spectra and core-loss spectra. Core-loss EELS spectra were calibrated by corresponding zero-loss EELS spectra before further analysis using a Digital Micrograph (Version 2.11, Gatan). STEM-HAADF images for 3D tomography were collected every 2° from −76° to +78°. 3D reconstruction was performed using Inspect 3D version 3.0 and was visualized using Amira 5.4.2.

Calculations. The first-principles structure and energy calculations were performed with the Vienna Ab Initio Simulation Package (VASP)[46,47]. To accurately describe the electronic structure, the hybrid Heyd–Scuseria–Ernzerhof (HSE06)[48] functional were used to calculate the energy and electronic structure. The HSE06 functional gives a good description of electronic properties such as bandgaps, formation enthalpies of LiMnO compounds and oxygen hole states[49]. In our calculation, the energy cutoff was set to 500 eV (1 × 1 × 2), and for the k-point, the Monkhorst–Pack scheme was used to sample the Brillouin zone. Full geometry optimizations were carried out with convergence thresholds of 1×10^{-4} eV and 5×10^{-3} eV Å^{-1} for total energy and ionic force, respectively. Both ions and lattices were relaxed in the primitive $Li_{15}Mn_7Ni_2O_{24}$ structure. Then, the defect structure was relaxed with a fixed supercell lattice. The spin polarization was included in the calculations, but only the ferromagnetic configuration was considered because the effect of different spin configurations on the formation energies is negligible[50,51]. It is well known that van der Waals (vdW) interactions are crucial in the determination of the equilibrium configurations in vdW structures, especially for LTMOs. Thus, the density functional theory–D3 approach was used to determine the effect of the vdW interaction[52]. In our calculations, the (2 × 2 × 1) $MnLi_2O_3$ supercell corresponded to $Mn_8Li_{16}O_{24}$. When one Mn atom and one Li atom in the layer of the Mn–O octahedral structure are replaced by two Ni atoms, it becomes a $Li_{15}Mn_7Ni_2O_{24}$ structure.

We first examined the valence states of both Mn and Ni ions in the $Li_{15}Mn_7Ni_2O_{24}$ structure. The partial DOS shows that some states exist above the Fermi level; these are mainly contributed by the Ni1 atoms. Thus, the divalent Ni^{2+} ion of Ni1 was oxidized to the trivalent ion, Ni^{3+}. The magnetic moments of Ni1 and Ni2 are 0.82 μ_B and 1.64 μ_B, which correspond to the electronic configuration of d7 (Ni^{3+}) and d8 (Ni^{2+}), respectively. The spin density of the Ni1 ion is provided by the d_Z^2 orbital, while the spin density of the Ni2 ion is provided by the d_Z^2 and d_x^2-y^2 orbitals.

During the charge process, Li ions are gradually released from the $Li_{15}Mn_7Ni_2O_{24}$. When two Li ions were released, the DOS and the corresponding partial charge of DOS in the $Mn_7Ni_2Li_{13}O_{24}$ structure indicate that the more-unoccupied orbitals of Ni atoms appear above the Fermi level. The detailed spin density and valence states of Ni1 and Ni2 ions become +4 and +3, respectively.

With further delithiation, all the Ni^{3+} ions gradually changes into 4+ ions. The DOS of $Li_9Mn_7Ni_2O_{24}$ shows that all of the Ni ions become 4+ ions, meanwhile three O holes, indicating an oxygen oxidation $O^{2-} \rightarrow O^- + e^-$ with the formation of oxygen holes, O^-. On further release of Li ions, the oxygen holes increase as the number of Li vacancies increase. The magnetic moments of Mn ions are almost unchanged as Li ions are released, which indicates that the valence states of all Mn ions remain unchanged.

The O^- hole state is known to be unstable in the solid state[53,54]. In bulk Li_2MnO_3 metal oxides, the reaction $O^- + O^- \rightarrow O_2^{2-}$ has a negative formation enthalpy[48]. The formation energy of oxygen vacancies (V_O) was calculated to determine the stability of O ions in the $Li_xMn_7Ni_2O_{24}$ structure. The formation energy of V_O is defined as follows:

$$E_f = E_{V_O} - E_{Mn_7Ni_2Li_xO_{24}} + u_O \quad (1)$$

where E_{V_O}, $E_{Li_xMn_7Ni_2O_{24}}$ and u_O represents the total energies of the $Li_xMn_7Ni_2O_{23}$ structure, the $Li_xMn_7Ni_2O_{24}$ structure and the chemical potential of the O atom, respectively. When the $Li_xMn_7Ni_2O_{24}$ structures contain O^- holes, the formation energies of V_O are greatly reduced from 4.87 eV for the initial configuration of $Li_{15}Mn_7Ni_2O_{24}$ to 1.31 eV for $Li_{15}Mn_7Ni_2O_{24}$ and $Li_3Mn_7Ni_2O_{24}$, respectively. Our studies of the energy, electronic structures and O^- hole states of $Li_xMn_7Ni_2O_{24}$ were based on HSE06 hybrid density functional calculations. As Li ions are released from the $Li_xMn_7Ni_2O_{24}$ structure, the valence states of Ni ions change from 2+ to 4+, and then O^- appears. The formation energies of V_O were greatly reduced due to formation of oxidized oxide ions (O^-).

Data availability

Data that support the findings of this study are kept at the William R. Wiley Environmental Molecular Sciences Laboratory at PNNL and are available from the corresponding authors upon request.

References

44. Kuppan, S., Shukla, A. K., Membreno, D., Nordlund, D. & Chen, G. Revealing anisotropic spinel formation on pristine Li- and Mn-rich layered oxide surface and its impact on cathode performance. *Adv. Energy Mater.* **7**, 1602010 (2017).
45. Devaraj, A. et al. Visualizing nanoscale 3D compositional fluctuation of lithium in advanced lithium-ion battery cathodes. *Nat. Commun.* **6**, 8014 (2015).
46. Kresse, G. & Furthmüller, J. Efficient iterative schemes for ab initio total-energy calculations using a plane-wave basis set. *Phys. Rev. B* **54**, 11169–11186 (1996).
47. Kresse, G. & Furthmüller, J. Efficiency of ab-initio total energy calculations for metals and semiconductors using a plane-wave basis set. *Comput. Mater. Sci.* **6**, 15–50 (1996).
48. Heyd, J., Scuseria, G. E. & Ernzerhof, M. Hybrid functionals based on a screened Coulomb potential. *J. Chem. Phys.* **118**, 8207–8215 (2003); erratum **124**, 219906 (2006).
49. Chen, H. & Islam, M. S. Lithium extraction mechanism in Li-rich Li_2MnO_3 involving oxygen hole formation and dimerization. *Chem. Mater.* **28**, 6656–6663 (2016).
50. Van der Ven, A., Aydinol, M. K., Ceder, G., Kresse, G. & Hafner, J. First-principles investigation of phase stability in Li_xCoO_2. *Phys. Rev. B* **58**, 2975–2987 (1998).
51. Xiao, R., Li, H. & Chen, L. Density functional investigation on Li_2MnO_3. *Chem. Mater.* **24**, 4242–4251 (2012).
52. Grimme, S., Antony, J., Ehrlich, S. & Krieg, H. A consistent and accurate ab initio parametrization of density functional dispersion correction (DFT-D) for the 94 elements H–Pu. *J. Chem. Phys.* **132**, 154104 (2010).
53. Chen, H. & Umezawa, N. Hole localization, migration and the formation of peroxide anion in perovskite $SrTiO_3$. *Phys. Rev. B* **90**, 035202 (2014).
54. Chen, S. & Wang, L.-W. Double-hole-induced oxygen dimerization in transition metal oxides. *Phys. Rev. B* **89**, 014109 (2014).